Volume 1 | Number 1 | Jan 2013 | Pages 1–100

Journal of
Materials Chemistry A

Materials for energy and sustainability
www.rsc.org/materialsA

Li⁺

e⁻

ROYAL SOCIETY
OF CHEMISTRY

ROYAL SOCIETY
OF CHEMISTRY

www.rsc.org/materialsA

ARTICLE TYPE

Halide Perovskite Materials for Solar Cells: A Theoretical Review

Wan-Jian Yin[a,b,*]**, Ji-Hui Yang**[a]**, Joongoo Kang**[a]**, Yanfa Yan**[b]**, and Su-Huai Wei**[a,*]

5 Halide perovskites have recently emerged as promising materials for low-cost, high-efficiency solar cells. The efficiency of perovskite-based solar cells has increased rapidly, from 3.8% in 2009 to 19.3% in 2014, by using the all-solid-state thin-film architecture and engineering cell structures with mixed-halide perovskites. The emergence of perovskite solar cells revolutionized the field not only because of their rapidly increased efficiency, but also flexibility in material growth and architecture. The superior
10 performance of the perovskite solar cell suggested that perovskite materials possess intrinsically unique properties. In this review, we summarize recent theoretical investigations into the structural, electrical, and optical properties of halide perovskite materials in relation to their applications in solar cells. We also discuss some current challenges of using perovskites in solar cells, along with possible theoretical solutions.

Introduction

15   Perovskites generally refer to a class of oxides with chemical formula ABO_3 that exhibit sought-after physical properties such as magnetic, ferroelectric, and two-dimensional
20 electronic conductivity.[1, 2] Recently, halide perovskites have drawn substantial interest in the fields of material research, as well as chemistry and physics.[3-15] This is due to the high efficiency of solid-state solar cells based on halide perovskite, which reached 17.9% in 2014,[16] up from 9.7% in 2012.[17] For
25 comparison, liquid-electrolyte solar cells had an efficiency of 3.8% in 2009.[11]

    Research into halide perovskites with chemical formula (A = 1+ ions or molecules, B = Ge, Sn, Pb, and X = I, Br, Cl), has existed for more than a century.[18] Their crystal structures as well
30 as ferroelectric behaviors were initially investigated about half a century ago.[19-25] However, the electricity-to-light conversion ability of halide perovskites, applied to light-emitting diodes (LED), was initially discovered by Mitzi's group in the 1990s[26-29] and such LEDs have only recently been fabricated[30]. Although
35 the light-to-electricity conversion (photovoltaic) process is the reverse of the electricity-to-light process, the first published report of using halide perovskites as solar cell absorbers emerged almost two decades later[11].

    In 2009 and 2006, Miyasaka *et al.*[11, 31] used organometallic
40 perovskites $CH_3NH_3PbI_3$ and $CH_3NH_3PbBr_3$ in dye-sensitized solar cells (DSSCs) and achieved efficiencies of 3.8% and 2.6%, respectively. By using $CH_3NH_3PbI_3$ nanoparticles and TiO_2 surface treatments, Park *et al.* achieved an efficiency of 6.5% in 2011,[32] creating a cell architecture similar to the extremely thin
45 absorber (ETA) DSSC. In 2012, due to the corrosion problems associated with liquid electrolytes, Park and Gratzel *et al.* replaced the liquid-based hole transport layer with solid-state spiro-MeOTAD and immersed perovskites into the TiO_2 scaffold. Unexpectedly, this increased the efficiency to 9.7%.[17] Using a
50 similar mesoscopic-structure architecture, Lee and Snaith *et al.*

achieved an efficiency of 7.6%.[9] They further found that the efficiency could be boosted to 10.9% when replacing electrically conducting TiO_2 with electrically inert Al_2O_3. Although there are still uncertainties related to the claim that Al_2O_3 performs better
55 than TiO_2, this finding indicated that perovskite itself might have efficient electrical transport properties. Following this clue, Liu and Snaith *et al.*[7] created efficient planar heterojunction perovskite solar cells using vapor deposition. The solar cell had no electron conductor scaffold other than a compact TiO_2 layer,
60 similar to thin-film solar cells. An efficiency of 15.4% was achieved with this architecture. Recently, Seok *et al.*[33] combined planar and scaffold layers of mixed-halide $CH_3NH_3Pb(I_{1-x}Br_x)_3$, and through fine-tuning the thickness ratio of planar and scaffold layers as well as chemical compositions, they achieved
65 consecutive record efficiencies from 16.2% to 17.9%.[16] Other developments include tuning perovskite properties with chemical compositions,[34, 35] developing efficient growth methods,[33, 36, 37] optimizing hole transport materials,[38-40] and engineering interface properties.[41, 42]

70   The superior performance of halide perovskite-based solar cells is reflected in their high open circuit voltage (V_{oc}). According to detailed balance theory,[43] the maximum V_{oc} (V_{oc-max}) of a semiconductor absorber is approximately its bandgap energy (E_g) subtracted by 0.3 eV. The ratio of V_{oc-max}/E_g indicates how
75 well the material will perform as a solar cell absorber. Table 1 lists record values for perovskite-based solar cells, with comparisons to several conventional solar cell absorbers. It is surprising that in terms of V_{oc-max}/E_g, perovskite-based solar cells is comparable to the $Cu(In,Ga)Se_2$ (CIGS) and superior to the
80 CdTe and $Cu_2ZnSn(S,Se)_4$ (CZTSS) based solar cells.

    Although theoretical investigations have not kept pace with experiments on halide perovskites, the basic electronic structures of halide perovskites were studied by first-principles calculations before the first perovskite solar cell was reported
85 experimentally. First-principles calculation based on density functional theory (DFT) is a computational modelling method

used to investigate the electronic structure of many-body systems. With this theory, the properties of a many-electron system can be determined by using density functionals, in which the exchange-correlation functional is the only not-well-defined. Therefore, different approximations of exchange-correlation functionals are used and may derive different results. Chang *et al.*[44] used local density approximation (LDA) to study cubic phase $CsPbX_3$ and $CH_3NH_3PbX_3$ (X = I, Br, Cl), and found that the hole effective mass was lighter than electron effective mass, which was not the case in conventional semiconductors. Borriello *et al.* [45] used generalized gradient approximation (GGA) to study organic and inorganic perovskites based on tin halide and found that the stability against the distortion of the perovskite cage strongly depends on the embedded cation. Recently, due to experimental progress, many theoretical investigations on structural and electronic properties of halide perovskite are emerging.[46-71] Different methodologies have been adopted, using exchange-correlation functionals such as LDA, GGA, hybrid functional methods (HSE), and quasiparticle GW methods. Other options include spin-orbit-coupling (SOC) and van der Waals interactions.

In this review, we summarize our recent theoretical investigations on halide perovskites[62, 63, 67, 70] and provide comparisons with existing theoretical and experimental work. The unique properties of halide perovskites were systematically investigated and explained as the origin of high performance in perovskite-based solar cells[62]. The dominating defects in halide perovskites were found not to be harmful because they do not create detrimental deep level within the bandgap,[63, 72] which could be carrier traps and recombination centers for electron-hole in solar cell. We also discuss how the stability and performance of perovskite solar cell may be improved from theoretical point of view.

Crystal structures

Perovskites, with formula ABX_3, typically have unit cells composed of five atoms in a cubic structure (α phase), where cation B has six nearest neighbor anions X and cation A has twelve (Figure 1(a)). Under ideal conditions, to maintain high-symmetry cubic structure, the ion radii of A, B, and X should satisfy the requirement that the tolerance factor t ($t = (R_A + R_X)/\{\sqrt{2}(R_B + R_X)\}$) should be close to 1, where R_A, R_B, and R_X are the ionic radii of corresponding ions. Otherwise, the cubic structure will be distorted and crystal symmetry is lowered. Of note, to satisfy t ≈ 1, the A ion must be much larger than the B ion. In halide perovskites, the B site is usually occupied by a large Pb or Sn atom, so A must be extremely large. Cs is almost the largest group-I element in the periodic table. However, Cs is still not large enough to hold the stable cubic perovskite structure, so it must be replaced with a larger molecule. This may be a reason that $CH_3NH_3PbI_3$ is more stable and performs better than $CsPbI_3$.

At finite temperature, a cubic structure may exist when t lies between 0.89 and 1.[73] Generally, smaller t could lead to the lower-symmetry tetragonal (β phase) or orthorhombic (γ phase) structures, whereas larger t (t>1) could destabilize the three-dimensional (3D) B-X network, leading to a two-dimensional (2D) layer structure. Notably, in DFT calculations at zero temperature, the γ phase is always the most stable, and the α phase is always the most unstable, because it is difficult to satisfy t=1. However, transitions between those structures at finite temperature often happen in most perovskites.[74, 75] In fact, the soft transverse acoustic phonon mode makes the anion X easily displaced from the B-B midpoint of the ideal cubic phase. At

finite temperature, such displacements are likely to be dynamic in nature.[74] Due to different ion sizes and structural stabilities, the transition temperatures of different perovskites vary. For the archetypal halide perovskite $CH_3NH_3PbI_3$, the α to β to γ phase transitions happens at 330 K and 160 K, respectively[76]. Interestingly, a non-perovskite δ phase was found for perovskites such as $HC(NH_2)_2PbI_3$, $FAPbI_3$, $CsPbI_3$ and $CsSnI_3$.[74, 75, 77] Unlike β and γ phases, the δ phase cannot be derived from α phase by B-X-B bond angle distortion. Instead, the B-X bond is broken (see Figure 1(d)).
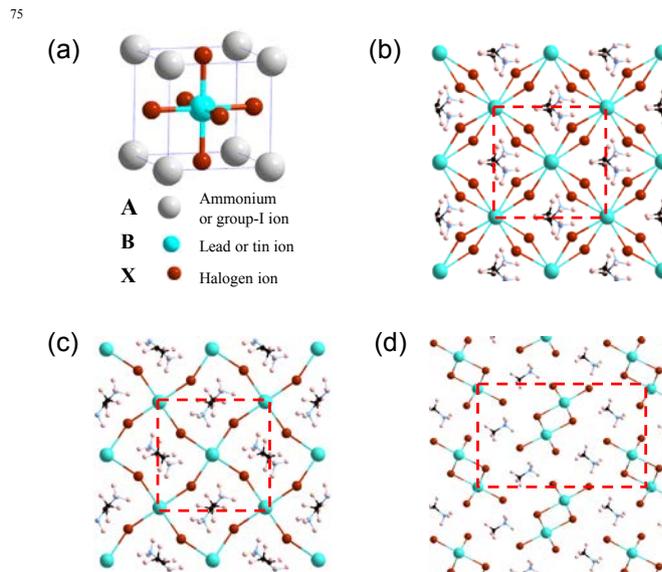

Figure 1: The atomic structure of (a) α phase, (b) β phase, (c) γ phase, and (d) δ phase $CH_3NH_3PbI_3$. The unit cells of β and γ phases are ($\sqrt{2} \times \sqrt{2} \times 2$), based on the α phase. Reprinted by permission from Ref. 62.

The atomic structures of organic-inorganic perovskites are more complicated than those of inorganic perovskites, because noncentrosymmetric organic molecules have many possible orientations. For $CH_3NH_3PbI_3$, the CH_3NH_3 molecules in the high-temperature α phase are randomly orientated and the overall crystals preserve O_h symmetry. In the medium temperature β phase, the freedom of CH_3NH_3 molecules are somewhat reduced but their orientations are still disordered. In the low-temperature γ phase, the CH_3NH_3 molecules are frozen and have fixed alignments.[74]

The disorder of the molecules' orientations in α and β phases is impossible to simulate in a finite unit cell. For α phase, we compared the total energies of $CH_3NH_3PbI_3$ with the C-N bond along [001], [110], and [111] directions and found that system is the most stable with a C-N bond along the [111] direction. The physical properties of α phase were calculated with the C-N bond along the [111] direction and the β phase is constructed accordingly. We note that other calculations show that [001] is the most stable direction, although their difference is very small. Also, the basic electronic structure of $CH_3NH_3PbI_3$ does not sensitively dependent on the direction of CH_3NH_3 molecule.

The calculated and experimental lattice parameters of α, β, γ and δ phases are shown in Table 2. We can see that generally LDA underestimates lattice parameters and GGA overestimates lattice parameters. This finding is consistent with the results for conventional semiconductors. However, for $CH_3NH_3PbI_3$, the overestimation of GGA(PBE)-calculated lattice parameters was attributed to the neglect of van der Waals interactions between

the CH$_3$NH$_3$ and [Pb-I] frameworks.[71] When dispersive interactions with particular form are considered, the calculated lattice parameters match experimental results well.[46, 47, 71] Based on this, the van der Waals interaction was claimed to be important fact in hybrid halide perovskites.[71] However, we posit that the importance of van der Waals interactions should be carefully revisited for two reasons. One, GGA/PBE overestimates lattice parameters not only for CH$_3$NH$_3$PbI$_3$ but also for other compounds, as this is an intrinsic problem of exchange-correlation functional not of particular material. Two, for inorganic CsPbI$_3$, when dispersive interaction is included, the calculated lattice parameters can also be in agreement with experimental ones.[46] Therefore, it could be that the GGA under-binds the compound. Adding dispersive interactions increases the binding of the compound and corrects GGA errors. It does not necessarily mean that dispersive interaction is intrinsic to halide perovskite. Corrections can also be achieved by mixing LDA and GGA, since LDA generally over-bind compounds. Following this reasoning, CH$_3$NH$_3$ behaves like an ion, and the interaction between CH$_3$NH$_3$ and [Pb-I] is similar to that between Cs and [Pb-I], which exhibits ionic character.

Electronic structures

We calculated the band structure, (partial) density of states (DOS) and partial charge density of valence band maximum (VBM) and conduction band minimum (CBM) states of α phase CH$_3$NH$_3$PbI$_3$ using DFT-PBE (Figure 2). The direct bandgap is at the R point. Unlike most cations whose outer *s* orbitals are empty, Pb has an occupied 6*s* orbital, which is below the top of valence bands of perovskites. This so-called lone pair of *s* electrons in Pb often gives rise to unusual properties.[78-80] DOS and partial charge density plots show that the VBM has strong Pb *s* and I *p* antibonding character, whereas the CBM is almost contributed from Pb *p* state, which reflects the unique dual nature (ionic and covalent) of halide perovskites' electronic structures. In conventional semiconductors such as GaAs and CdTe, the CBM primarily has *s* orbital character, whereas the VBM primarily has *p* orbital character. In contrast, halide perovskite exhibits inverted band structure. The state contributed by organic molecule is far from the band edges, which means that the organic molecule do not play a direct role in determining the basic electronic structures in halide perovskite. As discussed above, an important role of organic molecules in halide perovskites is stabilizing the perovskite structure and changing the lattice constant. Other possible effects of organic molecules, such as dipole polarization, are discussed later.

The band structures of β, γ, and δ phase CH$_3$NH$_3$PbI$_3$ are shown in Figure 3. The band structure of α phase with a ($\sqrt{2}\times\sqrt{2}\times2$) supercell is also shown for comparison. These calculations suggest that β and γ phases have band structures similar to α phase, which indicates that the Pb-I-Pb bond angle distortions do not significantly change the electronic structures. However, the band structure of δ phase is distinctive. The partial Pb-I bonds are broken and the 3D [Pb-I] framework is destroyed in the δ phase. In this phase, the coupling between Pb *s* and I *p* is weakened. As a result, the VBM, which is the *s-p* antibonding state, drops in energy, leading to an enlarged bandgap and a flat upper valence band. In experiments, the δ phase is usually yellow and has a bandgap of over 2 eV,[74, 75] i.e., more than 0.5 eV larger than that of the other phases. Its hole effective mass is expected to be much larger than that of other perovskite phases.
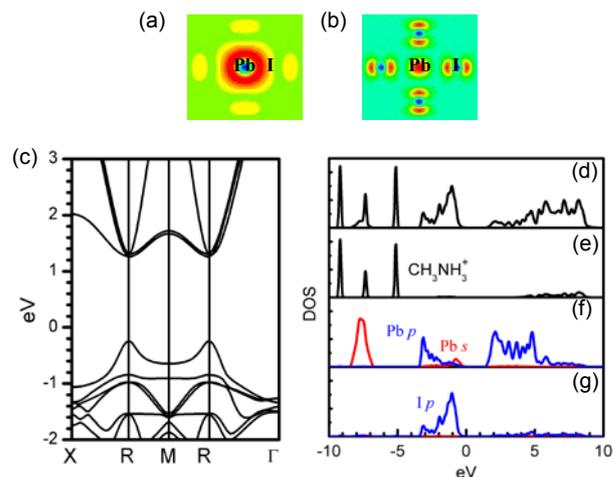

Figure 2: The (a) partial charge density of the CBM, (b) partial charge density of the VBM, (c) band structure, and (d) DOS of CH$_3$NH$_3$PbI$_3$ using DFT-PBE calculations. Modified by permission from Ref. 63.

The DFT-PBE calculated bandgap for β phase CH$_3$NH$_3$PbI$_3$ is 1.57 eV, which is in good agreement with experiments. However, this result is a fortuitous one, due to the accidental canceling-out of underestimating GGA and neglecting SOC.[66] This is not observed in other perovskites such as CH$_3$NH$_3$PbBr$_3$, CH$_3$NH$_3$PbCl$_3$ and CsPbI$_3$, whose GGA-calculated bandgaps are lower than experimental values. In those cases, advanced computational methods such as PBE+SOC,[66, 68] HSE+SOC,[81] and GW+SOC[57, 59, 60] have been used to study the electronic structure of CH$_3$NH$_3$PbI$_3$ and other perovskites. Notably, the key features of GGA-derived electronic structures, such as strong *sp* coupling and dual nature of bond characters, do not change with advanced methods. In fact, the SOC effect is not a unique finding for CH$_3$NH$_3$PbI$_3$. Heavy atoms such as Pb and Bi have large SOC effects, which also exists in semiconductors like PbTe[80] and Bi$_2$Se$_3$.[82] For those compounds, even though the band degeneracy and symmetry will change when SOC effect is included in calculations, the electronic structures and band character can be well described by non-SOC calculations.
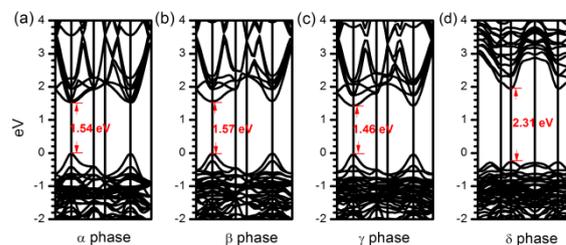

Figure 3: Band structure of (a) α phase, (b) β phase, (c) γ phase, and (d) δ phase CH$_3$NH$_3$PbI$_3$. α phase is calculated using the same tetragonal supercell as for β and γ phases. Reprinted by permission from Ref. 62.

Pb chalcogenides exhibit abnormal bandgap changes with lattice constant and strain.[80] Lang *et al.*[68] demonstrated that the bandgap increases from CsPbI$_3$, to CH$_3$NH$_3$PbI$_3$, to FAPbI$_3$. This is expected since the VBM has strong antibonding character and will drop when the lattice constant increases. However, the experimental bandgaps of CsPbI$_3$ (1.67 eV), CH$_3$NH$_3$PbI$_3$ (1.52 eV), and FAPbI$_3$ (1.48 eV) do not follow the theoretical trends. Furthermore, the trend is even more ambiguous when considering

bandgaps of CsSnI$_3$ (1.30 eV), CH$_3$NH$_3$SnI$_3$ (1.20 eV) and FASnI$_3$ (1.41 eV). Bandgaps' relations to lattice constant and crystal structures should be carefully revisited both in experiment and theory to address these uncertainties.

Ambipolar conductivity

The effective mass (m*) of electrons (holes) around the bottom of the conduction band (top of the valence band) can be approximately fitted by $m^* = \hbar^2 \left[\dfrac{\partial^2 \varepsilon(k)}{\partial^2 k} \right]^{-1}$, where $\varepsilon(k)$ are energy dispersion relation functions, which are typically described by band structures. Intuitively, the more dispersive (flat) the band near the band edges is, the lighter (heavier) the effective mass is. In conventional thin-film solar cell absorbers, such as GaAs and CdTe, the CBM is mostly contributed by cation s and anion s orbitals, and VBM is mostly contributed by anions' p character (p-s semiconductor). High-energy-level s orbitals are more delocalized than low-energy-level p orbitals and thus the lowest conduction band is more dispersive than the highest valence band. Consequently, the electron effective mass is much smaller than hole effective mass. That is why electrons transport much faster than holes, and why the second-generation thin-film solar cell must use p-type absorbers.

The existence of lone-pair Pb s electrons makes the situation dramatically different in perovskite solar cells. The electronic structure of CH$_3$NH$_3$PbI$_3$ is inverted compared to conventional p-s semiconductors. Its CBM is derived from Pb p orbitals, and the VBM is a mixture of Pb s and I p (s-p semiconductor) orbitals. Even though the CBM comes from p orbitals, a cation Pb p orbital has a much higher energy level than anion p orbitals, as in p-s semiconductors. Therefore, the lower conduction band of CH$_3$NH$_3$PbI$_3$ is more dispersive than the upper valence band in p-s semiconductors. On the other hand, due to strong s-p coupling around the VBM, the upper valence band of CH$_3$NH$_3$PbI$_3$ is dispersive. The DFT-PBE calculated electron and hole effective mass of α phase CH$_3$NH$_3$PbI$_3$, together with typical first and second-generation solar cell absorbers, are listed in Table 3. We can find that the hole effective mass of CH$_3$NH$_3$PbI$_3$ is balanced with the electron effective mass. The balanced effective mass in CH$_3$NH$_3$PbI$_3$ may lead to ambipolar conductivity[65] in perovskite solar cells, which facilitates the p-i-n junction solar cell. It is noted that the effective mass calculated by GW+SOC method[57] is even lower, indicating that many body effect may play a role for small carrier effective mass.

High optical absorption

One of the superior performance aspects of perovskite solar cells is high optical absorption, such that the absorber layer, which is less than 500 nm thick, can absorb enough sunlight to achieve high efficiency above 15%. The photoactive layer is even thinner since the mesoscopic absorber layer includes additional scaffold oxides (TiO$_2$, ZrO$_2$, or Al$_2$O$_3$). In comparison, the thickness of the absorber layers in first- and second-generation solar cells are about 300 μm and 2 μm, respectively.

First-principles calculations have been used to calculate the optical absorption of halide perovskites and to unravel the physics underlying this property. The optical absorption of a semiconductor is fundamentally determined by two factors. One is the transition matrix elements between valence band (VB) states and conduction band (CB) states, and the other is their joint density of states (JDOS). The former measures the probability of

each photoelectric transition, and the latter measures the total number of possible photoelectric transitions. Thus, the optical absorption coefficient of a material is closely related to its electronic structure.
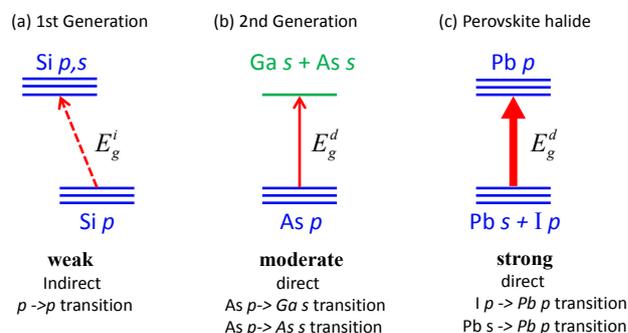

Figure 4: The schematic optical absorption of (a) first-generation, (b) second-generation, and (c) halide perovskite solar cell absorber. GaAs has been chosen as a prototypical second-generation solar cell absorber.
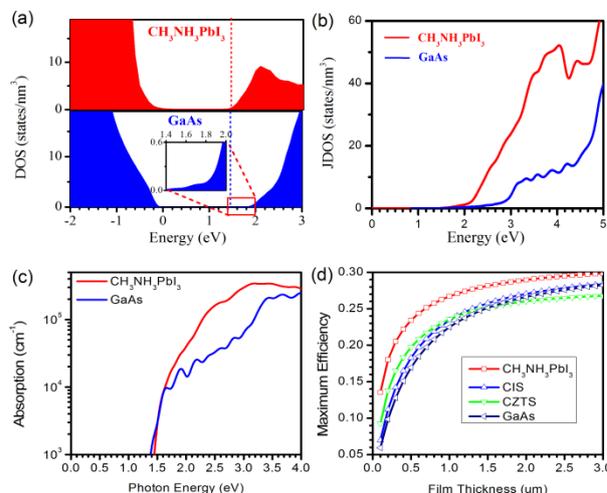

Figure 5: (a) Electronic density of states (DOS) of CH$_3$NH$_3$PbI$_3$ and GaAs. The VBMs are referred to as zero energy and CBMs are marked as dashed lines. (b) The JDOS of CH$_3$NH$_3$PbI$_3$ and GaAs. (c) The optical absorptions of CH$_3$NH$_3$PbI$_3$ and GaAs. (d) Calculated maximum efficiencies of CH$_3$NH$_3$PbI$_3$, CuInSe$_2$(CIS), Cu$_2$ZnSnS$_4$(CZTS), and GaAs as a function of film thickness. Modified by permission from Ref. 62.

The mechanisms of optical absorption for first-generation, second-generation, and perovskite-based solar cell absorbers are depicted schematically in Figure 4. For the first-generation absorber (silicon), the optical absorption close to the band edge is from the Si p orbital to the Si p and s orbitals. However, silicon is an indirect bandgap semiconductor and its transition probability between band edges are two orders lower than that of the direct bandgap, making its absorber layer two orders thicker and increasing the cost of materials. The bandgaps of the second-generation absorber (GaAs as example) and halide perovskite (CH$_3$NH$_3$PbI$_3$ as an example) are direct and thus their optical absorption is much stronger than that of silicon. However, the electronic structures of GaAs and CH$_3$NH$_3$PbI$_3$ are different. The

lower part of the GaAs CB is derived from the dispersive *s* band (delocalized *s* orbitals), whereas the lower part of the $CH_3NH_3PbI_3$ CB is mainly composed of degenerate Pb *p* bands. The atomic *p* orbital exhibits less dispersion than *s* orbitals do. As a result, the DOS in the lower CB of the halide perovskites is significantly higher than that of GaAs as shown in Figure 5(a), leading to a higher JDOS (Figure 5(b)). Additionally, the edge transition for $CH_3NH_3PbI_3$ comes from mixed-(Pb *s*, I *p*) to Pb *p* orbitals. The intra-atomic Pb *s* to Pb *p* transition probability is high, which makes the VBM-CBM transition probability of $CH_3NH_3PbI_3$ comparable to that of GaAs. Therefore, halide perovskites show stronger optical absorption than GaAs. The calculated optical absorption coefficients of $CH_3NH_3PbI_3$ and GaAs are shown in Figure 5(c). It is seen that the optical absorption coefficient of $CH_3NH_3PbI_3$ is up to 1 order of magnitude higher than that of GaAs within the visible light range. Because visible light accounts for the major usable portion of the full solar spectrum, high absorption in its range is critical for achieving high-efficiency cells.

Achieving high optical absorption is crucial for realizing economic and efficient solar cells with extremely thin absorbers. However, the effect of the optical absorption coefficient is not considered in the well-known Shockley-Queisser limit.[43] In a real-world solar cell, the theoretical maximum efficiency depends on the thickness of the absorber layer. Recently, Yu *et al.*[83, 84] took the absorption coefficient and absorber layer thickness into consideration and developed a method to calculate maximum efficiency based on absorber thickness. Using this approach, we have calculated the maximum efficiencies of perovskites and other mainstream thin-film absorbers. The results are shown in Figure 5(d)[62]. The halide perovskites ($CH_3NH_3PbI_3$ and $CsPbI_3$) exhibit much higher conversion efficiencies than GaAs, CIS, and CZTSe for any given thickness. More importantly, the halide perovskites are capable of achieving high efficiencies with very thin absorber layers. For example, with a 0.3 μm absorber (similar to the thickness of $CH_3NH_3PbI_{3-x}Cl_x$ in the 15.4 % perovskite-based cell[7]), $CH_3NH_3PbI_3$-based cells have a maximum efficiency of 21%, while it is only 13% for a GaAs-based solar cell. The results are consistent with many of today's most common thin-film solar cells (GaAs, CdTe, CIGS, and CZTSS)–the absorbers must be about 2 μm thick to achieve high efficiencies.[85]
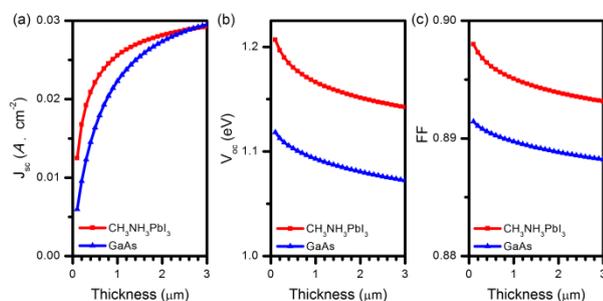

Figure 6: The calculated ideal device performances of (a) J_{sc}, (b) V_{oc}, and (c) FF for $CH_3NH_3PbI_3$- and GaAs-based thin-film solar cells as functions of thickness.

Following the idea of Yu *et al.*,[83, 84] we have also developed methods to calculate the thickness-dependent maximum solar cell parameters of $CH_3NH_3PbI_3$. Parameters such as short-circuit current (J_{sc}), open-circuit voltage (V_{oc}), and fill factor (FF) as a function of absorber thickness for $CH_3NH_3PbI_3$ and GaAs based thin-film solar cells are shown in Figure 6. The experimentally achieved J_{sc} (21.5 mA/cm²) and V_{oc} (1.07 eV) in $CH_3NH_3PbI_3$-based solar cells with a film thickness of 0.33 μm[7] are very close to our calculated theoretical limits for J_{sc} (19.2 mA/cm²) and V_{oc} (1.19 eV) at 0.30 μm. The bottleneck for present $CH_3NH_3PbI_3$-based solar cells is the relatively low FF (67%), which should be limited by the non-ideal band offsets between the perovskite absorber layer and the interfaces at the contact layer. Our results demonstrate that thin-film solar cells based on $CH_3NH_3PbI_3$ perovskite have the capability to achieve a high FF. Improved interfaces and contact layers in solar cells should significantly improve the cell performance, which is consistent with recent work on interface engineering and uniform growth to avoid the shunting resistance.

Superior point defect properties

In first- and second-generation solar cells, defect and doping properties were crucial factors affecting cell performance. The key component was the *pn* junction, where the photo-generated electrons and holes are separated and collected with the aid of the internal electric field. The *p* or *n*-type absorbers were made from materials with intrinsic defects, or using intentional doping. On the other hand, intrinsic defects that create deep energy levels in absorber usually act as Shockley-Read-Hall nonradiative recombination centers and carrier traps, reducing the carrier lifetime and thus V_{oc}. A good solar cell absorber must exhibit proper doping and defect properties. For example, the V_{oc} of a next-generation solar cell absorber, $Cu_2ZnSn(S,Se)_2$, is much lower than its bandgap, and its record efficiency is at about 12%.[85] This could be related to the energetically favorable formation of the dominating defect in $Cu_2ZnSnSe_2$, Cu_{Zn}, which can pin the *n*-type Fermi energy. It may also be due to the formation of a Sn_{Zn} deep level, which may become a carrier trap and nonradiative recombination center.[86, 87]
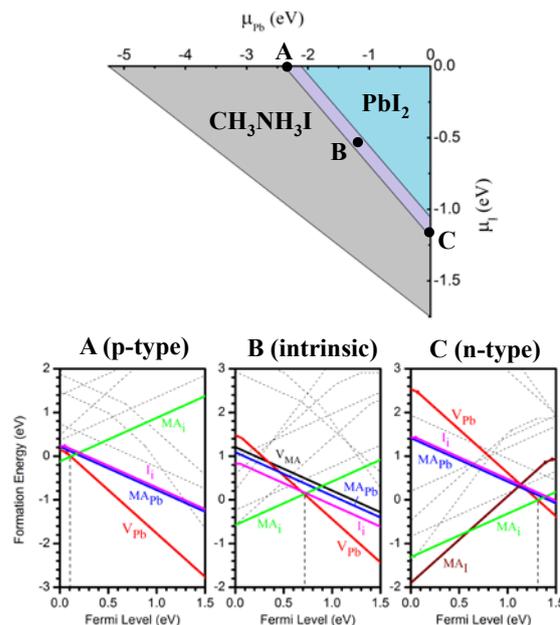

Figure 7: The achievable chemical potentials for thermo-equilibrium growth of $CH_3NH_3PbI_3$ and the formation energies of intrinsic point defects in $CH_3NH_3PbI_3$ at chemical potentials A, B, C. Defects with much higher formation energies are displayed as dashed lines. Modified by permission from Ref. 63.

It is still under debate whether a perovskite solar cell functions more like a dye-sensitized solar cell or thin-film solar cell. In a dye-sensitized solar cell, TiO_2 acts as an electron acceptor to aid electron transport. However, experiments by Snaith's group demonstrated that perovskite can transport electrons by itself, without scaffold TiO_2.[7, 9] Subsequent characterizations found both positive[88] and negative[89] effects of TiO_2 for solar cell function. Although the underlying mechanism of perovskite is unclear, point defects inevitably exist due to low-temperature solution based processes, making perovskites unintentionally doped. Interestingly, Laban and Etgar[90, 91] found p-type $CH_3NH_3PbI_3$ while You et al.[92] found n-type, meaning that $CH_3NH_3PbI_3$ is bipolarly dopable and different process can lead to opposite doping behaviors.

Several types of defects, including both donor-like and acceptor-like, exist in semiconductors. The relative concentrations of those donors and acceptors, which are directly related to the defect formation energies, determine p or n-type conductivity. The formation energy of a defect depends on the chemical potential μ, which corresponds to environmental factors such as precursors, partial pressure and temperature. In this way, the experimental conditions determine the formation energies of all the possible defects and thus impact the polar conductivity in the product material.
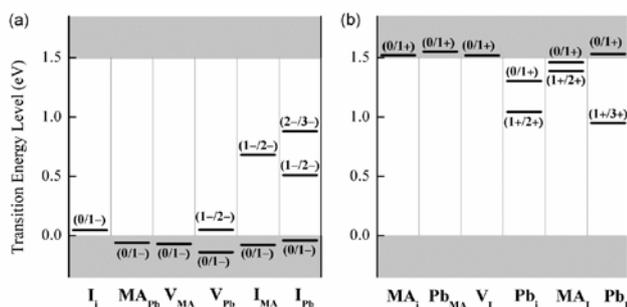

Figure 8: The transition energy levels of (a) intrinsic acceptors and (b) intrinsic donors in $CH_3NH_3PbI_3$. Zero in energy is referred to the VBM. Reprinted by permission from Ref. 63.

First-principles calculations have been used to study the point defect properties of α phase $CH_3NH_3PbI_3$.[63] The chemical potentials for equilibrium-growth are as shown in Figure 7(a), which indicates that growth of $CH_3NH_3PbI_3$ can occur only in a long and narrow range of chemical potential. Otherwise, secondary phases, such as PbI_2 and CH_3NH_3I would also form. Three typical chemical potentials (A, B, and C in Figure 7(a)) were chosen to study the formation energies of point defects. All the possible point defects, including three vacancies (V_{MA}, V_{Pb}, V_I), three interstitial (MA_i, Pb_i, I_i), two cation substitutions (MA_{Pb}, Pb_{MA}) and four antisite substitutions (MA_I, Pb_I, I_{MA}, I_{Pb}), were considered in our calculations. The formation energies of these point defects as a function of Fermi level position at chemical potentials A, B, and C are shown in Fig. 7 (b), (c), and (d) respectively. The lowest crossing points between donor and acceptor indicate the positions of Fermi level pinning. The conductivity of $CH_3NH_3PbI_3$ can arise from intrinsically good p-type conduction, but interestingly, it can also arise from moderate to good n-type conduction when the chemical potential is at A(I-rich/Pb-poor), B (moderate), or C (I-poor/Pb-rich). Such flexible defect properties are distinct from those of conventional thin-film solar cell absorber CIGS[93] and CZTSS.[94] This is due to the chemical similarity of the cations and the presence of Cu

antibonding d orbitals at the VBM, which means that acceptors such as V_{Cu}, Cu_{Ga}, and Cu_{Zn} have very low formation energies. Thus, in equilibrium growth, p-type doping in CIGS and CZTSS is easy but n-type doping is difficult due to self-compensation.[93] In $CH_3NH_3PbI_3$, the dominant donor MA_i and dominant acceptor V_{Pb} have comparable formation energies, so both p-type and n-type doping are possible in $CH_3NH_3PbI_3$. Our theoretical results on bipolar conductivities are consistent with the experimental findings of both p and n-type $CH_3NH_3PbI_3$ in different growth processes.

Defect formation energies determine the polar conductivity of a semiconductor, whereas defect transition levels determine the electrical effect of any particular defect. The transition level of a defect is the Fermi level position where the defect can gain or lose electrons and change its charge state. Shallow defect levels, close to band edges, can donate or accept electrons to bulk bands and become effective doping methods for absorbers. However, deep levels defects, near the middle of the bandgap, can trap electrons or holes and become SRH nonradiative recombination centers in the absorber. The transition levels of all possible point defects in $CH_3NH_3PbI_3$ are shown in Figure 8. The defects with low formation energies, as shown in solid lines in Figure 7(b-d), have transition energies less than 0.05 eV above (below) VBM (CBM). All defects that create deep levels have high formation energies, as shown in dashed lines in Figure 7(b-d). Besides point defects, Kim et al.[64] used DFT-GGA to calculate the DOS and partial charge densities of two types of neutral defects in β phase $CH_3NH_3PbI_3$: Schottky defects (equal numbers of positive and negative vacancies) and Frenkel defects (equal numbers of vacancies and interstitials of the same ion). They found that those defect pairs do not create deep gap states. Du[81] used DFT-PBE calculations and similarly found that in β phase $CH_3NH_3PbI_3$, most of the point defects are shallow. Alternatively, he found that for I interstitial, a particular configuration may be a deep state, with a role in electrical properties. So far, it is not clear whether the deep I interstitial state in Du's calculation is derived from different crystal phases or particular defect structures.

Shallow defect properties are closely related to the dual-nature electronic structures of halide perovskites. The shallow dominant acceptors V_{Pb} and MA_{Pb} originate from covalent coupling between the Pb lone-pair s and I p orbitals, which increases the VBM so that the acceptors are generally shallower than in cases without strong sp coupling. The mechanism is similar for the shallow V_{Cu} in CIGS, where the VBM is increased by coupling between the Cu d and Se p orbitals.[93] The shallow donors MA_i and V_I are due to the high ionicity. The MA_i has no covalent bonds to the Pb-I framework and does not create additional gap states. For V_I, our previous study has shown that weak covalence generally leads to the shallow anion vacancy levels.[95]

Figure 9: The proposed hole-conductor-free perovskite solar cell without HTM layer by utilizing p-type doping.

The tunable polar conductivity and shallow defect properties may help explain why high-performance perovskite solar cells, with extremely long carrier lifetimes,[96, 97] can be produced by a diverse range of growth approaches and a wide variety of solar cell architectures. The superior point defect properties would suggest new architectures for perovskite solar cell architecture. The two prevailing architectures are mesoscopic and planar structures. The former mostly used porous TiO_2 to help electron transport while the latter do not. Both need a hole transport material (HTM) layer to support hole transportation from the perovskite absorber to contact. Organic HTM materials are expensive and many researchers are seeking inorganic materials as economic substitutes,[98-100] even though they generally do not behave as well as organic ones. However, the HTM layers are not necessary if the absorber can be effectively *p*-type doped as proposed in our theory above. In this case, the HTM layer would be replaced by the *p*-type perovskite layers. Electron and holes can be separated through an intrinsic *p-i-n* junction, as depicted in Figure 9. Recently, several reports[91, 101-103] have been published on the effective performance of hole-conductor-free perovskite solar cells, demonstrating the potential applications of *p-i-n* homojunctions in solar cells. Alternatively, Agiorgousis *et al.*[104] found that deep point defect levels could exist through large atomic relaxations which they attributed to the strong covalency of the system.

Electrically benign structural disorder

Most of the current theoretical studies on halide perovskites are based on ordered structures such as α, β, and γ phases. However, perovskite structures in real devices have been found to be disordered and complicated[105]. In a mesoscopic-structure solar cell, the optically active perovskites are integrated into a mesoporous network of TiO_2 or Al_2O_3, where the majority of the layers is optically inert scaffold oxide. Experimentally, it is difficult to determine the structure of minor perovskite embedded within the oxides' irregular pores using conventional crystallographic methods. Recently, Choi *et al.*[105] reported the first fully quantitative structural characterization of $CH_3NH_3PbI_3$ within mesoporous TiO_2 using atomic pair distribution analysis of high energy X-ray diffraction. They found that most of $CH_3NH_3PbI_3$ (70%) is highly disordered with local perovskite structure extending over a range of only 1.4 nm, which is about 2 lattice constants of α phase. The mesoporous scaffold confined the perovskite within the pores and reshaped the structures of perovskites. On the other hand, the low-temperature growth process inevitably leads to polycrystalline perovskite with grain boundaries (GBs). Currently, there are no experimental investigations on the structural and electronic properties of those structural disorders and topological defects, because high-quality material is required for high resolution transmission spectroscopy (HRTEM), and the organic molecule in halide perovskite could be easily broken under a high-energy electron beam. Alternatively, theoretical calculations[69] can provide direct insights into the electrical properties of structural disorders and topological defects in hybrid perovskites.

In conventional polycrystalline light absorbers, GBs could dramatically alter the electronic and optical properties from those of the single-crystal phase. GBs are usually detrimental to solar cell performance. For example, our recent first-principle calculations showed that many intrinsic GBs in solar cell absorbers CdTe,[106, 107] $CuInSe_2$,[108] and $Cu_2ZnSnSe_2$[109] create deep defect levels in the bandgaps, acting as carrier traps and nonradiative recombination centers that harm carrier lifetime and

device performance in solar cells. We further found that the detrimental intrinsic GB behaviors in thin-film solar cell absorbers originated from the formation of undesirable chemical bonds, especially anion-anion bonds at the structural core of GBs. To reduce these detrimental activities, specific post-processing treatments are required for polycrystalline silicon, CdTe, and CIGS cells. For example, Cl-treatment in experiments enhanced the efficiency of CdTe solar cells. Recent combined theoretical and experimental studies[106] have demonstrated that Cl segregated into the GB part of polycrystalline CdTe solar cell, effectively taming the detrimental effects at GBs. In addition, unintentional passivation at GBs by defect segregations has been shown to be important in high-efficiency CIGS[108] and CZTS[109] solar cells. Therefore, solar cells based on polycrystalline thin-film semiconductors often require intentional or unintentional passivation to achieve improved carrier lifetime and V_{oc}. Interestingly, high-efficiency perovskite solar cells may not require such treatment. Edri *et al.*[110] measured the electron beam induced current (EBIC) on as-grown $CH_3NH_3PbI_3$ and found that the EBIC contract from the GBs of polycrystalline $CH_3NH_3PbI_3$ sample is not different from that of grains themselves, indicating negligible charge separation and recombination occurred at GBs. According to their results, GBs in $CH_3NH_3PbI_3$ are almost electrically invisible. It is unclear whether such benign GB properties are intrinsic, or arise from other effects such as unintentional defect segregations. We therefore investigated what causes such different GB properties in perovskites versus conventional thin-film absorbers.
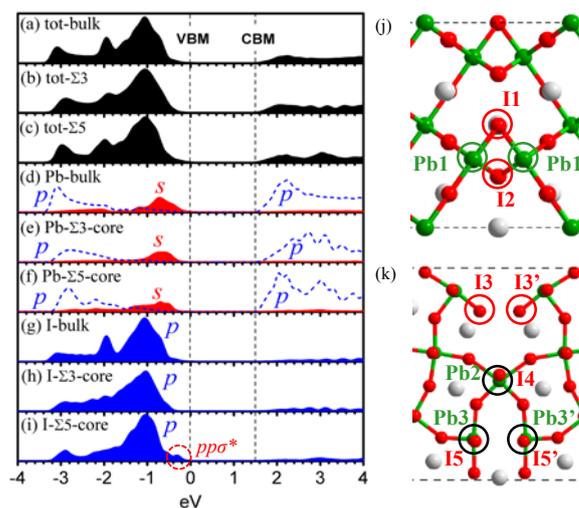

Figure 10: (a-i) are (partial) DOS of pristine $CsPbI_3$ and polycrystalline $CsPbI_3$ with Σ3(111) and Σ5(310) GBs. (j) and (k) are atomic structures at Σ3(111) and Σ5(310) GBs respectively.

We used first-principles calculations to investigate the electronic properties of GBs in halide perovskites. We chose two types of GBs as indicated in Figure 10 as model systems, because those structures are low-energy and have been observed in large abundance in $SrTiO_3$, a model perovskite oxide. Both are rich in disordered configurations such as distorted bond angles, I-I wrong bonds, Pb dangling bonds, and I dangling bonds. Thus they represent the general features of GBs in polycrystalline perovskites.

Due to the structural complicity of $CH_3NH_3PbI_3$, the GBs structures were constructed based on $CsPbI_3$. The DOS of those GBs are shown in Figure 10(a-i) and compared to that of single-

crystal phase CsPbI$_3$. We can see that the DOSs of the supercells with GBs are very similar to those of single-crystal phases. None of these GBs introduce defect states within the bandgap region. The results, therefore, suggest that GBs in halide perovskites are electrically benign. Such intrinsically clean GB behaviors have not been seen in other solar cell absorbers such as CdTe,[107] CuInSe$_2$,[108] and Cu$_2$ZnSnSe$_4$.[109]

The electrically benign nature of GBs in halide perovskites is closely related to their electronic structures. The origin of the deep gap state in CdTe GBs, with comparisons to halide perovskites, is shown in Figure 11. Te-Te wrong bonds at the GBs in CdTe introduce deep defect levels, which are the antibonding $pp\sigma^*$ states of the Te-Te bond. Similarly, in the perovskites, the I-I wrong bonds also create antibonding $pp\sigma^*$ states in Σ5(311) GB. However, the $pp\sigma^*$ state is not as deep as in CdTe. There are two reasons for this. First, the VBM in halide perovskite is much higher than I $5p$, because strong Pb $6s$ and I $5p$ coupling significantly increases the VBM level. Higher VBM means shallower defect levels. Second, the I-I interaction in halide perovskite is weaker than the anion-anion interaction in chalcogenides due to the larger distances for the I-I pair. As evidence, the Se-Se bond length in the CZTSe Σ3(114) GB is 2.50 Å,[109] which is much shorter than the I-I bond length (3.70 Å) at the Σ5(310) GB in CsPbI$_3$. Also, the Se-Se bond length is 1.11 times of the ionic size of Se^{2-}, whereas the I-I bond length is 1.48 times of ionic size of I^{1-}.
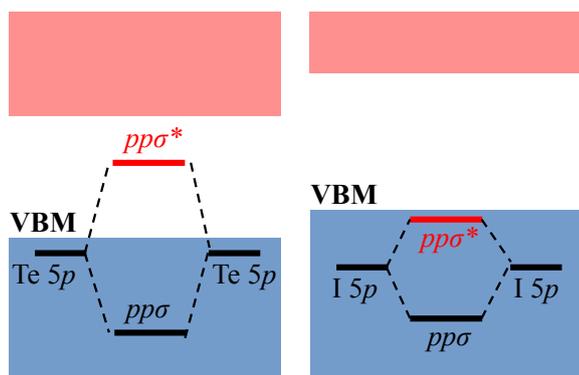

Figure 11: The schematic diagrams of defect state formation at CdTe and perovskite GBs.

The large I-I bond length in halide perovskites is a consequence of its extremely large lattice constant due to the previously mentioned large A and B atoms in halide perovskites. As discussed, A should be larger than B due to the structural stability requirement. In Pb-based perovskites, the Pb atom at the B site is large, and the Cs atom or CH$_3$NH$_3$ molecule at the A site is even larger. Reduced anion-anion interatomic coupling could partly explain why large cations are necessary in perovskite for high-performance solar cells. It was noted in a previous report[111] that increasing the lattice parameter by applying the tensile strain at GB of CuInSe$_2$ can effectively push the anion-anion antibonding $pp\sigma^*$ level below the VBM, so that the GB becomes electrically benign. The relatively compact structures of CIS with smaller atoms mean that the wrong bond interactions at GBs are much stronger, creating deep level defects. In perovskites, large atomic sizes and loose crystal structures weaken the wrong bonds at GBs, leading to intrinsically benign GBs .

Ferroelectric effect

Another evident difference between organic-inorganic hybrid perovskite and conventional inorganic absorber is the dipole moment of the noncentrosymmetric organic cation. Frost *et al.* [56] calculated the electronic dipole of the organic cation in halide perovskites and showed that hybrid perovskites exhibit spontaneous electric polarization, and proposed that the presence of ferroelectric domains will result in internal junctions that may aid electron-hole separation and transportation.

The spontaneous electric polarization in halide perovskites may have two origins. One is the alignment of the dipole moments of organic cations, and the other is intrinsic lattice distortion breaking the crystal centrosymmetry. The calculated magnitude of the CH$_3$NH$_3$PbI$_3$ bulk polarization, using the Berry phase method, is 38 μC/cm^2, which is comparable to the value of ferroelectric oxide perovskite such as KNbO$_3$ (30 μC/cm^2)[56]. We note that for ferroelectric perovskite oxides-based solar cell V$_{oc}$ can be larger than the bandgap, and charge separation and carrier lifetime can be enhanced due to the internal electric field.[112]
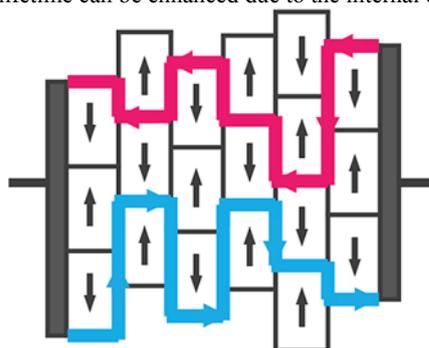

Figure 12: The schematic diagrams of ferroelectric multidomains as hypothesized in halide perovskite solar cells. The diffusion highways for carriers are indicated by red and blue lines and arrows. Reprinted by permission from Ref. 56.

For halide perovskites-based solar cell, Frost *et al.*[56] proposed that the boundaries of ferroelectric domains may form "ferroelectric highways" that facilitate the transportation of electrons and holes as shown in Figure 12. Within each domain, where the polarization direction is fixed, electrons and holes can be effectively separated along the direction of electric field before they can recombine. Crucially, these ferroelectric boundaries are peaks and troughs in electrostatic potential, where electrons and holes automatically choose distinct energetically favorable "highways", avoiding any "collision" with the opposite charge. Such an effect may be another unique property of halide perovskites and recent experiment[113] claimed direct observation of ferroelectric domains in β phase CH$_3$NH$_3$PbI$_3$.

Interface and Surface

Although the bulk properties of the absorber is crucial for its solar cell performance, the surface and interface between absorber, carrier transport layers, and electrode contact layers are also important for efficient carrier transportation. Newly developed growth processes including the two-step methods,[8] vacuum deposition, and vapor-assisted solution processing methods,[36] have improved on the quality yielded by the one-step method. These methods improved the uniformity of interfaces and prevented direct contact between hole and electron

transportation layers. To further improve solar cell performance, there are at least three aspects worth consideration.

First is band alignment. The proper band alignments between spiro-MeTAD and perovskites as well as perovskites and TiO$_2$ make spiro-MeTAD and TiO$_2$ good candidates for carrier transportation. When photo-excited electrons and holes are generated at CBs and VBs of perovskite as in Figure 13, the electrons will move to the CB of TiO$_2$, while the holes will move to the VBs of the HTM layer. In a dye-sensitized solar cell, the carrier transportations between different layers in solar cells are driven by the band-offset induced electrostatic potential difference near the interfaces. Typical band offsets are schematically shown as Δ_i in Figure 13. For Δ_1 and Δ_2, overly small band offsets will not facilitate the effective carrier transportation whereas overly large band offsets could reduce the V$_{oc}$. For Δ_3 and Δ_4, small values are required to avoid further reduction of V$_{oc}$ while keeping efficient carrier extraction. Recently, Zhou *et al.*[41] optimized the interface by manipulating the interface band alignments. They replaced unintentionally-doped TiO$_2$ with yttrium-doped TiO$_2$ (Y-TiO$_2$) and used low work-function ITO to replace high work-function FTO, under the hypothesis that Y-TiO$_2$ could enhance the electron extraction from perovskites as well as electron transport within TiO$_2$. This suppressed carrier recombination in the perovskite absorber, facilitated carrier injection into the carrier transport layers, and maintained good carrier extraction at the electrode. As a result, they achieved cell efficiencies up to 19.3%.

The bandgaps and band alignments of perovskites can also be tuned by chemical management of compositional elements, including organic cations,[102, 114] Pb,[35, 115] and halogen elements.[34, 116, 117] This is another way to optimize band alignment at interfaces. Currently, the exact energies of band alignments between different layers of materials are unclear. For example, the experimentally reported Δ_1 and Δ_2 values in Figure 13 are 0.07-0.25 eV and 0.11-0.33 eV, respectively.[32, 33, 41, 91, 99, 101, 118-120] Band alignment calculations are also scarce. First-principle calculations may help identify the optimized materials at interfaces through chemical doping/alloying of oxides or perovskite absorbers.

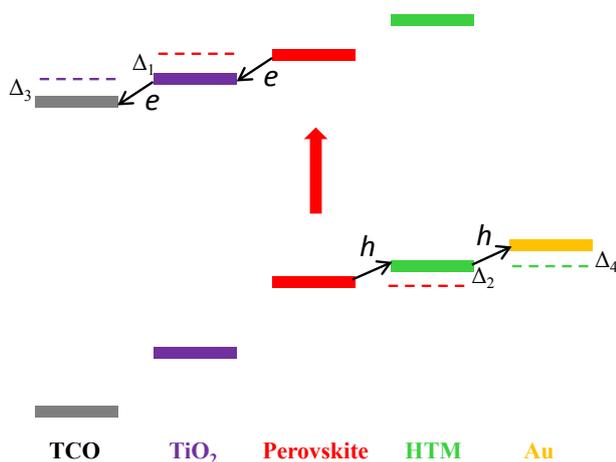**TCO   TiO$_2$ Perovskite   HTM   Au**

Figure 13: A schematic band diagram of different functional layers in perovskite solar cell. The band alignments affecting cell performance are marked as Δ_i. The band alignments are not to scale and show only the relative positions.

A second factor is interface structure and passivation. The atomic structures at an interface between two materials with different symmetries are complicated, prone to defects, dangling bonds, and wrong bonds. Those structural deficiencies could introduce deep defect states within bandgap and act as charge traps or recombination centers. The unusual hysteresis of I-V curve of perovskites solar cell,[121, 122] which would reduce the working cell efficiency, was suspected to be related to the interface properties. Mosconi *et al.*[54] used first-principles calculation to study the electronic properties of interfaces between TiO$_2$ and β phase CH$_3$NH$_3$PbI$_3$. They found that CH$_3$NH$_3$PbI$_3$ tended to grow in a (110)-oriented film on TiO$_2$, due to better structural matching. Cl was found to enhance the binding energy and thus had stronger modification of interface electronic structure, leading to a stronger interfacial coupling and to a slight TiO$_2$ CBM upshift. It seems that no deep defect states were found at TiO$_2$/CH$_3$NH$_3$PbI$_3$ interface, which is consistent with experimental observations that the TiO$_2$/CH$_3$NH$_3$PbI$_3$ interface is more electrically active than the CH$_3$NH$_3$PbI$_3$/HTM interface.[110, 123] EBIC measurements and surface photovoltage spectroscopy also indicated high electron recombination velocities at this interface. The poor CH$_3$NH$_3$PbI$_3$/HTM interface may be why HTM-free perovskite solar cells perform well. Thus, engineering the CH$_3$NH$_3$PbI$_3$/HTM interface is crucial, but as of yet there is no theoretical investigation, or available guidelines .

The third factor is surface, which is related to the interface. Abate *et al.* [124] reported the existence of trap states at the perovskite surface, which generated charge accumulation and consequent recombination losses in working solar cells. They identified undercoordinated iodine ions as responsible, and used supramolecular halogen bond complexation for passivation. After passivation, their solar cell demonstrated a maximum power conversion efficiency of 15.7%. On the other hand, the first-principles calculation by Haruyama *et al.* [55] suggested that the electronic structures of various surfaces of β phase CH$_3$NH$_3$PbI$_3$, including (110), (001), (100), and (101) surfaces largely retain the characteristics of bulk CH$_3$NH$_3$PbI$_3$. The discrepancies suggest a need for reevaluations of surface properties, both theoretical and experimental. Interestingly, Socampo *et al.* [119] found that the higher cell performance can be achieved by growing tetragonal CH$_3$NH$_3$PbI$_3$ with the long axis parallel to the substrate, which can be realized by temperature control during growth process. This experimental finding is consistent with Mosconi's theoretical prediction of (110)-oriented perovskite film on TiO$_2$.[54]

Mixed-halide perovskites

Chemical management of compositional elements[34, 35, 59, 61, 101, 116, 117] have been verified as effective methods for refining the properties of CH$_3$NH$_3$PbI$_3$. In general, mixing halides in perovskite has at least three beneficial effects. The first is increasing stability. Lee *et al.*[9] found that perovskites CH$_3$NH$_3$Pb(I$_{1-x}$Cl$_x$)$_3$ was remarkably stable during processing in air, compared to CH$_3$NH$_3$PbI$_3$. Noh *et. al.*[34] demonstrated that mixing 20%-29% Br into CH$_3$NH$_3$PbI$_3$ greatly improved the solar cell stability. The second is enhancing carrier transport. CH$_3$NH$_3$Pb(I$_{1-x}$Cl$_x$)$_3$ demonstrated much longer electron-hole diffusion length than CH$_3$NH$_3$PbI$_3$[96, 97, 110, 116]. Improved carrier mobility and reduced carrier recombination rates were also observed in CH$_3$NH$_3$Pb(I$_{1-x}$Br$_x$)$_3$[125] and CH$_3$NH$_3$Pb(Br$_{1-x}$Cl$_x$)$_3$[126]. The third is bandgap tuning. CH$_3$NH$_3$PbBr$_3$[127] (CH$_3$NH$_3$PbBr$_{3-x}$Cl$_x$[126]) have achieved V$_{oc}$ up to 1.3 eV (1.5 eV) and can be used to create colorful solar cell designs for energy-saving buildings. The consecutive bandgap range of mixed halide perovskites CH$_3$NH$_3$Pb(I$_{1-x}$Cl$_x$)$_3$, CH$_3$NH$_3$Pb(I$_{1-x}$Br$_x$)$_3$ and CH$_3$NH$_3$Pb(Br$_{1-x}$Cl$_x$)$_3$ could also be used for application in multi-junction solar

cells[125-127]. Solar cells using $CH_3NH_3Pb(I_{1-x}Br_x)_3$ as the light harvester reached 17.9% efficiency in early 2014, the current certified record[16].

Solar cells using mixed-halide perovskites may potentially achieve efficiencies above 20%. However, there are many fundamental issues that need addressing, especially the stability and miscibility between different halide perovskites. For example, the atomic ratio of Cl in $CH_3NH_3PbI(_{1-x}Cl_x)_3$ was previously assumed to be up to one third, as it is in precursors.[9, 61] However, recent experiments[76, 116] show that its atomic ratio is less than 4% and most of the precursor Cl may be sublimated. Therefore, the miscibility of Cl into iodine should be carefully studied. We used first-principle calculations[128] together with Monte-Carlo simulations based on cluster expansion methods (CEM)[129, 130] to systematically study the structural, electronic, and energetic properties of mixed-halide β phase $CsPbX_3$ (X=I, Br, Cl). The alloy structures were constructed based on special-quasirandom-structure (SQS) within a 160-arom supercell. Computational details have been previously published.[70] The volumes, formation energies, and bandgaps of those SQS alloys generally follow the parabolic shape and their fitting curves are shown in Figure 14. The formation energies, ΔH, of alloys in Figure 14(b) generally follow $\Delta H = \Omega x(1-x)$. A higher interaction parameter Ω indicates that the alloys are more difficult to form. The calculated Ω values (averaged per halogen atom) for $CsPb(I_{1-x}Cl_x)_3$, $CsPb(I_{1-x}Br_x)_3$, and $CsPb(Br_{1-x}Cl_x)_3$ are 113 meV, 40 meV and 21 meV respectively. The trend of interaction parameters for $CsPb(I_{1-x}Cl_x)_3$, $CsPb(I_{1-x}Br_x)_3$, and $CsPb(Br_{1-x}Cl_x)_3$ follow the trend of ionic size difference between Cl^- (1.67 Å), Br^- (1.84 Å), and I^- (2.07 Å). The miscibility gap temperature at x=1/2, $T_{MG}(x=1/2)$, can be estimated by $T_{MG} = \Omega/(2k_B)$,[131] where k_B is the Boltzmann constant. In this way, the miscibility gap temperatures of $CsPb(I_{1-x}Cl_x)_3$, $CsPb(I_{1-x}Br_x)_3$, and $CsPb(Br_{1-x}Cl_x)_3$ were calculated to be 625 K, 223 K and 116 K. Since the growth temperature of $CH_3NH_3PbX_3$ is usually below 450 K, our results indicate that mixed-(Br,Cl) and mixed-(I,Br) perovskites could be easily formed, but not mixed-(I,Cl) perovskites. For bandgaps, the experimental results for $CH_3NH_3Pb(I_{1-x}Br_x)_3$ and $CH_3NH_3Pb(Br_{1-x}Cl_x)_3$ are shown in Figure 14 (c), which are overall in agreement with our theoretical calculations. For $CH_3NH_3Pb(I_{1-x}Br_x)_3$, Noh et al.[34] observed a bandgap bowing parameter of 0.33 eV. However, Suarez et al.[125] found almost zero bandgap bowing, which is close to our theoretical value of -0.01 eV based on SQS.
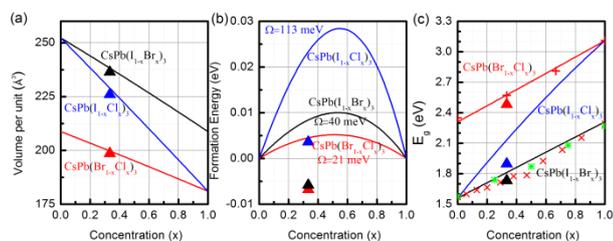

Figure 14: The (a) volumes, (b) formation energies (per halogen atom), and (c) bandgaps of the mixed halide alloys $CsPbX_{1-x}Y_x$ (X, Y = I, Br, Cl) by SQS calculation. The solid lines are fitted by calculated results of SQS at nine different concentrations (fitted points not shown). The results of the stable ordered structures at x=1/3 are shown as triangles. For bandgaps, the available experimental data are given (red cross marks are from Ref. 132, red plus marks are from Ref. 34, and green star marks are from Ref. 125). The small deviations between experiment and theory may indicate that in the experimental samples the atomic

distribution is not perfectly random. Reprinted by permission from Ref. 70.

Another interesting finding from our study is a particularly stable alloy structure at x = 1/3, where x is the concentration of the perovskite with a smaller lattice constant. Its structure is shown in Figure 15(a). Monte-Carlo simulations demonstrated that the formation energies of this structure deviate significantly from the parabolic trend and are much lower than in other structures. The unusual stability at x = 1/3 may be understood as the combined effect of strain energy and Coulomb energy.

In conventional semiconductor alloys, the formation energies are positive and generally follow $\Delta H = \Omega x(1-x)$. Such energy mostly comes from the strain energy by which the ideal A and B bulks are stretched or compressed due to the lattice constant of alloy $A_{1-x}B_x$. Usually, a small lattice constant results in a larger bulk modulus, meaning it is relatively hard to mix large atoms into bulks with a small lattice constant, and easy to mix small atoms into bulks with a large lattice constant. As a result, the maximum value for alloy formation energy is not at x = 0.5, but falls closer to the small lattice constant bulk as seen in Figure 15(b). The formation energies of conventional semiconductor alloys, especially for covalent system such as $GaAs_{1-x}Sb_x$,[133] follow the strain energies well. However, halide perovskites have strong ionic character, thus Coulomb interactions should play an important role.
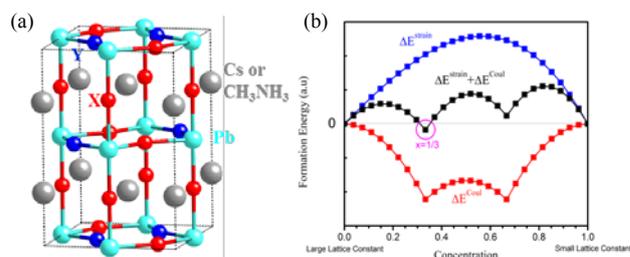

Figure 15: (a) Our found stable structure at x=1/3. (b) The contributions of strain energy and Coulomb energy in the alloy. Reprinted by permission from Ref. 70.

For example, consider $CsPb(I_{1-x}Cl_x)_3$. Due to the electronegativity difference between I and Cl, an I electron will partially transfer to Cl, making Cl more negatively charged than I. In this case, Coulomb energy, modulated by different orders of (I,Cl) structure, could play an important role in total energy. According to cluster expansion methods (CEM),[129, 130] the screened Coulomb energy is approximately proportional to the averaged spin product $\left\langle \overline{\Pi}_{(2,1)} \right\rangle$ for anion-anion nearest neighbors.

The spin products in CEM reflect the structural orders in alloys, thus the minimized average spin product $\left\langle \overline{\Pi}_{(2,1)} \right\rangle$ in an ionic alloy system corresponds to a particular ordered structure that minimizes the Coulomb energy. Here, the amount of Coulomb energy gain was calculated as the difference between the lowest $\left\langle \overline{\Pi}_{(2,1)} \right\rangle$ at particular ordered structures and $\left\langle \overline{\Pi}_{(2,1)} \right\rangle$ at random structures at various concentrations. The lowest $\left\langle \overline{\Pi}_{(2,1)} \right\rangle$ at ordered structures was derived by minimizing $\left\langle \overline{\Pi}_{(2,1)} \right\rangle$ using Monte-Carlo simulations and $\left\langle \overline{\Pi}_{(2,1)} \right\rangle$ at random structure was given by $(2x-1)^2$.[129, 130] The calculated Coulomb energy gain is shown in Figure 15(b). We can see that the alloy system get the largest Coulomb energy gain at concentration x=1/3 and 2/3. The

crystal structure with lowest $\left\langle \overline{\prod}_{(2,1)} \right\rangle$ at x=1/3 is shown in Figure 15(a), where each Y (blue) ion has maximum (8) nearest neighbors of X (red) anion to minimize $\left\langle \overline{\prod}_{(2,1)} \right\rangle$. In this particular crystal structure, Coulomb energy gain is maximized.

Considering both strain energies and Coulomb energies, we found that the formation energies of mixed halide perovskite had a minimum at x=1/3 (close to bulk with large lattice constant) as depicted in black lines in Figure 15(b). Previous DFT-GGA calculations[61] found different stable structure of $CH_3NH_3PbI_2Cl$ where Cl is at the apical site. Here, for the given unit cell, we found the new structure in Figure 15(a) is more stable by 60 meV per formula unit than previous structure. More interestingly, the calculated formation energies of $CsPb(I_{2/3}Br_{1/3})_3$, $CsPb(I_{2/3}Cl_{1/3})_3$, and $CsPb(Br_{2/3}Cl_{1/3})_3$ of the new structure were -5 meV, 4 meV, -7 meV per formula unit respectively. Negative formation energies indicate that the perovskite structure can be stabilized by adding halides. Noh *et al.*[34] found that $CH_3NH_3PbI_{3-x}Br_x$-based solar cells exhibit long-term stability at x=0.20 and 0.29, which are close to our prediction of x=1/3 for stable $CsPbI_{3-x}Br_x$. Cl addition into $CH_3NH_3PbI_3$ has also been shown to increase structural stability,[7, 9] carrier diffusion length,[96, 97, 116, 125] and solar cell efficiency. Based on our theoretical investigations, we encourage the further study of stabilized mixed-halide perovskites.

Halide perovskites other than $CH_3NH_3PbI_3$

Although most work on perovskite in solar cell applications has focused on $CH_3NH_3PbI_3$, there is an ongoing search for other candidates. Concerns for commercializing $CH_3NH_3PbI_3$ include lead toxicity, a suboptimal bandgap, and long-term stability. Researchers have modified the elemental composition of $CH_3NH_3PbI_3$ to address those concerns.

The reported bandgaps of $CH_3NH_3PbI_3$ are between 1.50 eV and 1.61 eV in literature. However, the optimal bandgap for a single-junction solar cell is between 1.1 eV and 1.4 eV. Perovskite solar cell efficiencies can be further improved by searching for smaller bandgap perovskites. As discussed, the main role of the cation CH_3NH_3 is stabilizing perovskite structure. In principle, there are many other choices, such as Cs, NH_4, $C_2H_5NH_3$, and $HC(NH_2)_2$. $CsPbI_3$, NH_4PbI_3 and $C_2H_5NH_3PbI_3$ all have larger bandgaps than $CH_3NH_3PbI_3$. $HC(NH_2)_2PbI_3$ (FAPbI$_3$) has a smaller bandgap of 1.48 eV. FAPbI3-based solar cells have achieved an efficiency of 14.2% and their carrier lifetime is as good as cells using $MAPbI_{3-x}Cl_x$.[99, 134] Thermogravimetric measurements on MA- and FA-based perovskites by Hanusch *et al.*[135] indicated that FAPbI$_3$ is more thermally stable than both MAPbBr$_3$ and MAPbI$_3$, which is consistent with the finding that a larger cation at A site could further stabilize perovskite structure.

Efforts at making Pb-free perovskite by replacing toxic Pb with other group IVA elements such as Ge and Sn have been attempted. MASnI$_3$ and CsSnI$_3$ can be grown experimentally, and have optimal bandgaps of 1.3 eV.[35, 74, 77, 136, 137] Ge-based perovskites such as CsGeCl$_3$ and MAGeCl$_3$ can also be synthesized.[74] However, the stability of the 2+ state decreases from Pb, to Sn, to Ge, which presents a considerable problem. For instance, Sn^{2+} in Sn-based perovskites easily oxidizes to Sn^{4+} in the atmosphere. However, $CH_3NH_3SnI_3$-based solar cells have been made by encapsulating the device under an inert atmosphere, and an efficiency up to 6% has been found,[136, 137] demonstrating that Pb-free perovskite solar cells are possible. In addition, a mixed-(Sn,Pb) perovskite, $MAPb_{1-x}Sn_xI_3$, could reduce the amount of used Pb, while tuning the bandgap and retaining stability.[35, 115] The electronic properties and stabilities of Sn-related perovskite and mixed-(Sn,Pb) perovskite should be further studied.

Another possibility is using MAPbBr$_3$ and MAPbCl$_3$, which have larger bandgaps than MAPbI$_3$, as the top layer for tandem perovskite solar cells.[127] MAPbBr$_3$-based solar cells have demonstrated V_{oc} up to 1.5 eV.[126, 138] Using a mixed-halide perovskite can tune the bandgap, as well as increase the carrier mobility and structural stability.

Conclusions and prospect

In this paper, the authors review the current understanding of the perovskite materials and their applications in solar cells. First-principles calculations have been proven to be powerful methods for studying the electronic, optical, and defect properties of perovskites, and providing atomistic explanations and guidance for experiments. Theoretical results have demonstrated that halide perovskites exhibit a series of superior electronic and optical properties for solar cell application, such as proper bandgap and band alignment, high optical absorption, bipolar carrier conductivity, tunable doping ability, and benign defect properties.

Theoretical studies can address a number of other aspects of perovskites' behavior in solar applications. One is anomalous hysteresis in perovskite solar cells.[122] Frost *et al.*[52] have proposed that the dipole moment of organic cation could contribute to the hysteresis, although recent experiments suggested that grain sizes and interface may play an important role[139], which requires further investigation. Further first-principles investigations are needed to optimize the material's properties, and to find new perovskite candidates for high-efficiency, stable solar cells. As previously mentioned, the bandgap of archetypal halide perovskite $CH_3NH_3PbI_3$ is larger than the ideal. Band structure engineering of $CH_3NH_3PbI_3$ could be extensively investigated by replacing organic cations, Pb, or I with other choices. Furthermore, the mechanisms of performance degradations are still not well studied, even though long-term stability is a crucial aspect of commercialization. Rapid degradation in moist environments have suggested that water may corrode perovskites. The chemical reactions between H_2O and the perovskite surface could be carefully studied to unravel the reaction mechanism, leading to the development of methods for stabilizing perovskite. Long-term stable perovskite solar cells have recently been fabricated in laboratory through chemical composition engineering.[34, 101, 114] However, the fundamental reason for alloy stabilizing of the structures requires more study. Overall, first-principles calculations will continue to have an important role in the understanding and development of the emerging technology of perovskite solar cells.

Table 1. The room temperature bandgaps (Eg), open-circuit voltage (Voc), short-circuit current (JSC), Fill factor (FF) and efficiency (η) of GaAs-, CIGS-, CdTe-, CZTSS-, $CH_3NH_3PbI_3$-based solar cells. Both the experimental achieved and theoretical maximum values by Shockley-Queisser limit are shown for comparison.

	E_g (eV)		V_{OC} (V)	Voc/Voc-max	J_{SC} (mA/cm^2)	J_{SC}/Jsc-max	FF (%)	FF/FF-max	η (%)
GaAs	1.43	Exp	1.12	95.7%	29.68	94.0%	86.5	96.6%	28.8
		SQ-limit	1.17		31.56		89.5		33.0
CIGS	1.14	Exp	0.752	83.9%	35.3	82.5%	77.2	88.5%	20.5
		SQ-limit	0.896		42.81		87.2		33.5
CdTe	1.44	Exp	0.872	73.9%	29.47	94.6%	79.5	88.7%	20.4
		SQ-limit	1.18		31.16		89.6		32.8
CZTSS	1.13	Exp	0.513	57.8%	35.2	81.3%	69.8	80.1%	12.6
		SQ-limit	0.887		43.3		87.1		33.4
$CH_3NH_3PbI_3$	1.55	Exp	1.07	83.6%	21.50	79.0%	68.0	75.4%	15.4
		SQ-limit	1.28		27.20		90.2		31.4

Table 2. The calculated lattice constants and band gaps of the three phases of $CH_3NH_3PbX_3$ (X=I, Br, Cl) are compared with the experimental ones. Because the CH_3NH_3 molecule is noncentrosymmetric, for α phase, the calculated pseudocubic lattice constant is defined by $a=V^{1/3}$ and for β phase, $a = \frac{1}{2}(a+b)$. The relative total energy (meV/formula), referred to α phase, is also given. For HSE+SOC, 43% portion of exact-exchange is chosen to reproduce the band gap of β phase $CH_3NH_3PbI_3$ as in Ref. 81. Reprinted by permission from Ref. 70.

Phase	Symmetry	Lattice constant (Å)		Relative energy (meV)			Band gap (eV)			
		PBE	Exp	PBE	PBE+SOC	HSE+SOC	PBE	PBE+SOC	HSE+SOC	Exp
$CH_3NH_3PbI_3$										
α	$Pm\bar{3}m$	a=6.39	a=6.31[75], 6.28[74]	0	0	0	1.53	0.46	1.14	
β	$I4/mcm$	a=8.80, c=12.99	a=8.85[74, 75], 8.88[116], c=12.64[75], 12.67[116]	-93	-127	-100	1.57	0.77	1.60	1.52[75], 1.5[17],
γ	$Pbnm$	a=8.84, b=8.77, c=12.97	a=8.84[74], b=8.56[74], c=12.58[74],	-38	-55	-50	1.46	0.59	1.43	
$CH_3NH_3PbBr_3$										
α	$Pm\bar{3}m$	a=6.04	a=5.94[34], a=5.95[132],	0	0	0	1.93	0.89	1.92	2.23[117], 2.32[127], 2.29[34, 125], 2.35[132]
β	$I4/mcm$	a=8.28, c=12.25		-60	-59	-92	1.98	1.13	2.11	
γ	$Pbnm$	a=8.32, b=8.29 , c=12.15		-21	-19	-44	1.81	0.91	1.86	
$CH_3NH_3PbCl_3$										
α	$Pm\bar{3}m$	a=5.78	a=5.70[129]	0	0	0	2.40	1.33	2.57	3.11[132]
β	$I4/mcm$	a=7.93, c=11.71		-52	-53	-65	2.47	1.57	2.77	
γ	$Pbnm$	a=7.94, b=7.95, c=11.66		-12	-16	-18	2.27	1.31	2.47	

Table 3. DFT-PBE calculated effective masses for electrons and holes.

	Electron effective mass (m_e)	Hole effective mass (m_e)
CH$_3$NH$_3$PbI$_3$	0.35, 0.32[65]	0.31, 0.36[65]
CH$_3$NH$_3$PbI$_3$ (SOC)	0.18, 0.23[65]	0.21, 0.29[65]
CsSnI$_3$	0.19	0.09
CsSnI$_3$ (SOC)	0.16	0.07
Silicon	0.26	0.29
GaAs	0.07	0.34
CuInSe$_2$	0.09	0.75
Cu$_2$ZnSnSe$_4$	0.10	0.26
CdTe	0.09	0.28

Notes and references

aNational Renewable Energy Laboratory, Golden, CO 80401, USA
bDepartment of Physics and Astronomy, University of Toledo, OH 43606, USA
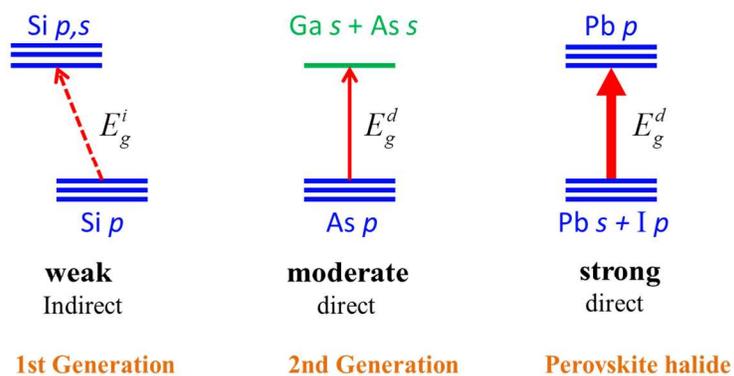5 *Corresponding Author: Wan-Jian Yin and Su-Huai Wei,*
E-mail: wan-jian.yin@nrel.gov, suhuai.wei@nrel.gov

1. R. E. Cohen, *Nature*, 1992, **358**, 136-138.
2. M. A. Pena and J. L. G. Fierro, *Chemical Reviews*, 2001, **101**, 1981-
10   2017.
3. P. Gao, M. Gratzel and M. K. Nazeeruddin, *Energy & Environmental Science*, 2014, **7**, 2448-2463.
4. S. A. Bretschneider, J. Weickert, J. A. Dorman and L. Schmidt-Mende, *Apl Mater*, 2014, **2**, 040701.
15 5. H. J. Snaith, *J Phys Chem Lett*, 2013, **4**, 3623-3630.
6. N.-G. Park, *J Phys Chem Lett*, 2013, **4**, 2423-2429.
7. M. Liu, M. B. Johnston and H. J. Snaith, *Nature*, 2013, **501**, 395-+.
8. J. Burschka, N. Pellet, S.-J. Moon, R. Humphry-Baker, P. Gao, M. K. Nazeeruddin and M. Graetzel, *Nature*, 2013, **499**, 316-+.
20 9. M. M. Lee, J. Teuscher, T. Miyasaka, T. N. Murakami and H. J. Snaith, *Science*, 2012, **338**, 643-647.
10. I. Chung, B. Lee, J. He, R. P. H. Chang and M. G. Kanatzidis, *Nature*, 2012, **485**, 486-U494.
11. A. Kojima, K. Teshima, Y. Shirai and T. Miyasaka, *Journal of the*
25   *American Chemical Society*, 2009, **131**, 6050-+.
12. N.-G. Park, *Materials Today*, 2014, DOI: 10.1016/j.mattod.2014.07.007.
13. M. A. Green, A. Ho-Baillie and H. J. Snaith, *Nature Photonics*, 2014, **8**, 506-514.
30 14. M. Gratzel, *Nature Materials*, 2014, **13**, 838-842.
15. M. D. McGehee, *Nature Materials*, 2014, **13**, 845-846.
16. http://www.nrel.gov/ncpv/images/efficiency_chart.jpg
17. H.-S. Kim, C.-R. Lee, J.-H. Im, K.-B. Lee, T. Moehl, A. Marchioro, S.-J. Moon, R. Humphry-Baker, J.-H. Yum, J. E. Moser, M. Graetzel
35   and N.-G. Park, *Scientific Reports*, 2012, **2**, 591.
18. H. L. Z. Wells, *Anorg. Chem.*, 1893, **3**, 195.
19. K. Yamada, K. Isobe, E. Tsuyama, T. Okuda and Y. Furukawa, *Solid State Ionics*, 1995, **79**, 152-157.
20. W. Depmeier, A. Moller and K. H. Klaska, *Acta Crystallographica*
40   *Section B-Structural Science*, 1980, **36**, 803-807.
21. B. Winkler, V. Milman and M. H. Lee, *J Chem Phys*, 1998, **108**, 5506-5509.
22. C. K. Moller, *Nature*, 1958, **182**, 1436.
23. A. N. R. S. E. Christensen, *Acta Chem. Scand.*, 1965, **19**, 421.
45 24. C. K. Moller, *Nature*, 1957, **180**, 981.
25. D. Weber, *Z. Naturforsh*, 1978, **33b**, 1443.
26. D. B. Mitzi, K. Chondroudis and C. R. Kagan, *Ibm Journal of Research and Development*, 2001, **45**, 29-45.
27. D. B. Mitzi, *Journal of the Chemical Society-Dalton Transactions*,
50   2001, **1**, 1-12.
28. D. B. Mitzi, *Chem Mater*, 2001, **13**, 3283-3298.
29. D. B. Mitzi, S. Wang, C. A. Feild, C. A. Chess and A. M. Guloy, *Science*, 1995, **267**, 1473-1476.
30. Z.-K. Tan, R. S. Moghaddam, M. L. Lai, P. Docampo, R. Higler, F.
55   Deschler, M. Price, A. Sadhanala, L. M. Pazos, D. Credgington, F. Hanusch, T. Bein, H. J. Snaith, R. H. Friend, *NATURE NANOTECHNOLOGY*, 2014, **9**, 687-692.
31. A. T. Kojima, K.; Shirai, Y., *Proc. 210th ECS Meeting (ECS, 2006)*,
      2006, Abstract #397.
60 32. J.-H. Im, C.-R. Lee, J.-W. Lee, S.-W. Park and N.-G. Park, *Nanoscale*, 2011, **3**, 4088-4093.
33. N. J. N. Jeon, J. H.; Kim, Y. C.; Yang, W. S.; Tyu, S.; Seok S. I., *Nature Materials*, 2014, **13**, 897-903.
34. J. H. Noh, S. H. Im, J. H. Heo, T. N. Mandal and S. I. Seok, *Nano*
65   *Lett*, 2013, **13**, 1764-1769.
35. Y. Ogomi, A. Morita, S. Tsukamoto, T. Saitho, N. Fujikawa, Q. Shen, T. Toyoda, K. Yoshino, S. S. Pandey, T. L. Ma and S. Hayase, *J Phys Chem Lett*, 2014, **5**, 1004-1011.
36. Q. Chen, H. P. Zhou, Z. R. Hong, S. Luo, H. S. Duan, H. H. Wang,
70   Y. S. Liu, G. Li and Y. Yang, *Journal of the American Chemical Society*, 2014, **136**, 622-625.
37. J. J. Shi, Y. H. Luo, H. Y. Wei, J. H. Luo, J. Dong, S. T. Lv, J. Y. Xiao, Y. Z. Xu, L. F. Zhu, X. Xu, H. J. Wu, D. M. Li and Q. B. Meng, *Acs Applied Materials & Interfaces*, 2014, **6**, 9711-9718.
75 38. N. J. Jeon, J. Lee, J. H. Noh, M. K. Nazeeruddin, M. Gratzel and S. I. Seok, *Journal of the American Chemical Society*, 2013, **135**, 19087-19090.
39. N. J. Jeon, H. G. Lee, Y. C. Kim, J. Seo, J. H. Noh, J. Lee and S. I. Seok, *Journal of the American Chemical Society*, 2014, **136**, 7837-
80   7840.
40. D. Q. Bi, L. Yang, G. Boschloo, A. Hagfeldt and E. M. J. Johansson, *J Phys Chem Lett*, 2013, **4**, 1532-1536.
41. H. P. Zhou, Q. Chen, G. Li, S. Luo, T. B. Song, H. S. Duan, Z. R. Hong, J. B. You, Y. S. Liu and Y. Yang, *Science*, 2014, **345**, 542-
85   546.
42. Q. Chen, H. P. Zhou, T. B. Song, S. Luo, Z. R. Hong, H. S. Duan, L. T. Dou, Y. S. Liu and Y. Yang, *Nano Lett*, 2014, **14**, 4158-4163.
43. W. Shockley and H. J. Queisser, *J Appl Phys*, 1961, **32**, 510.
44. Y. H. Chang, C. H. Park and K. Matsuishi, *Journal of the Korean*
90   *Physical Society*, 2004, **44**, 889-893.
45. I. Borriello, G. Cantele and D. Ninno, *Phys Rev B*, 2008, **77**, 235214.
46. Y. Wang, T. Gould, J. F. Dobson, H. M. Zhang, H. G. Yang, X. D. Yao and H. J. Zhao, *Physical Chemistry Chemical Physics*, 2014, **16**, 1424-1429.
95 47. J. C. Menendez-Proupin E.; Palacios P.; Wahnon P.; Conesa, *Phys Rev B*, 2014, **90**, 045207.
48. R. Gottesman, E. Haltzi, L. Gouda, S. Tirosh, Y. Bouhadana and A. Zaban, *J Phys Chem Lett*, 2014, **5**, 2662-2669.
49. G. Murtaza, I. Ahmad, M. Maqbool, H. A. R. Aliabad and A. Afaq,
100   *Chinese Physics Letters*, 2011, **28**, 117803.
50. G. Murtaza and I. Ahmad, *Physica B-Condensed Matter*, 2011, **406**, 3222-3229.
51. X. Zhu, H. Su, R. A. Marcus, M. E. Michel-Beyerle, *J Phys Chem Lett*, 2014, **5**, 3061.
105 52. F. Brivio, A. B. Walker, and A. Walsh, *Apl Mater*, 2014, **2**, 081506.
53. T. Minemoto and M. Murata, *J Appl Phys*, 2014, **116**, 054505.
54. E. Mosconi, E. Ronca and F. De Angelis, *J Phys Chem Lett*, 2014, **5**, 2619-2625.
55. J. S. Haruyama, K.; Han L.; Tateyama Y., *J Phys Chem Lett*, 2014, **5**,
110   2903.
56. K. T. B. Jarvist M. Frost, Federico Brivio, Christopher H. Hendon, Mark van Schilfgaarde, and Aron Walsh, *Nano Lett*, 2014, **14**, 2584.

57. F. Brivio, K. T. Butler, A. Walsh, and M, van Schilfgaarde, *Phys Rev B*, 2014, **89**, 155204.

58. F. Brivio, A. B. Walker and A. Walsh, *Apl Mater*, 2013, **1**, 042111.

59. A. Amat, E. Mosconi, E. Ronca, C. Quarti, P. Umari, M. K. Nazeeruddin, M. Gratzel and F. De Angelis, *Nano Lett*, 2014, **14**, 3608-3616.

50. P. Umari, E. Mosconi and F. De Angelis, *Scientific Reports*, 2014, **4,** 4464.

61. E. Mosconi, A. Amat, M. K. Nazeeruddin, M. Gratzel and F. De Angelis, *J Phys Chem C*, 2013, **117**, 13902-13913.

62. W.-J. Yin, T. Shi and Y. Yan, *Advanced Materials*, 2014, **26**, 4653-4658.

63. W. J. Yin, T. Shi and Y. Yan, *Appl Phys Lett*, 2014, **104**, 063903.

64. J. Kim, S. H. Lee, J. H. Lee and K. H. Hong, *J Phys Chem Lett*, 2014, **5**, 1312-1317.

65. G. Giorgi, J. I. Fujisawa, H. Segawa and K. Yamashita, *J Phys Chem Lett*, 2013, **4**, 4213-4216.

66. J. Even, L. Pedesseau, J. M. Jancu and C. Katan, *J Phys Chem Lett*, 2013, **4**, 2999-3005.

67. A. Filippetti and A. Mattoni, *Phys Rev B*, 2014, **89**, 125203.

68. L. Lang, J. H. Yang, H. R. Liu, H. J. Xiang and X. G. Gong, *Phys Lett A*, 2014, **378**, 290-293.

69. W. -J.Yin, H. Y. Chen, T. Shi, S.-H. Wei, and Y. Yan, unpublished.

70. W. -J. Yin, Y. Yan, and S.-H. Wei, *J Phys Chem Lett*, **5**, 3625-3631. .

71. D. A. Egger and L. Kronik, *J Phys Chem Lett*, 2014, **5**, 2728-2733.

72. J. Miller, *Physics Today*, 2014, **67**, 13.

73. C. H. Li, X. G. Lu, W. Z. Ding, L. M. Feng, Y. H. Gao and Z. G. Guo, *Acta Crystallographica Section B-Structural Science*, 2008, **64**, 702-707.

74. T. Baikie, Y. N. Fang, J. M. Kadro, M. Schreyer, F. X. Wei, S. G. Mhaisalkar, M. Graetzel and T. J. White, *Journal of Materials Chemistry A*, 2013, **1**, 5628-5641.

75. C. C. Stoumpos, C. D. Malliakas and M. G. Kanatzidis, *Inorg Chem*, 2013, **52**, 9019-9038.

76. J. M. Ball, M. M. Lee, A. Hey and H. J. Snaith, *Energy & Environmental Science*, 2013, **6**, 1739-1743.

77. I. Chung, J. H. Song, J. Im, J. Androulakis, C. D. Malliakas, H. Li, A. J. Freeman, J. T. Kenney and M. G. Kanatzidis, *Journal of the American Chemical Society*, 2012, **134**, 8579-8587.

78. A. Walsh and G. W. Watson, *Journal of Solid State Chemistry*, 2005, **178**, 1422-1428.

79. A. Walsh, D. J. Payne, R. G. Egdell and G. W. Watson, *Chemical Society Reviews*, 2011, **40**, 4455-4463.

80. S. H. Wei and A. Zunger, *Phys Rev B*, 1997, **55**, 13605-13610.

81. M. H. Du, *Journal of Materials Chemistry A*, 2014, **2**, 9091-9098.

82. H. J. Zhang, C. X. Liu, X. L. Qi, X. Dai, Z. Fang and S. C. Zhang, *Nature Physics*, 2009, **5**, 438-442.

83. L. P. Yu and A. Zunger, *Physical Review Letters*, 2012, **108**, 068701.

84. L. P. Yu, R. S. Kokenyesi, D. A. Keszler and A. Zunger, *Advanced Energy Materials*, 2013, **3**, 43-48.

85. M. A. Green, K. Emery, Y. Hishikawa, W. Warta and E. D. Dunlop, *Progress in Photovoltaics*, 2014, **22**, 701-710.

86. A. Polizzotti, I. L. Repins, R. Noufi, S. H. Wei and D. B. Mitzi, *Energy & Environmental Science*, 2013, **6**, 3171-3182.

87. S. Y. Chen, J. H. Yang, X. G. Gong, A. Walsh and S. H. Wei, *Phys Rev B*, 2010, **81**, 245204.

88. Y. X. Zhao, A. M. Nardes and K. Zhu, *J Phys Chem Lett*, 2014, **5**, 490-494.

89. C. S. Ponseca, T. J. Savenije, M. Abdellah, K. B. Zheng, A. Yartsev, T. Pascher, T. Harlang, P. Chabera, T. Pullerits, A. Stepanov, J. P. Wolf and V. Sundstrom, *Journal of the American Chemical Society*, 2014, **136**, 5189-5192.

90. L. Etgar, P. Gao, Z. Xue, Q. Peng, A. K. Chandiran, B. Liu, M. K. Nazeeruddin and M. Graetzel, *Journal of the American Chemical Society*, 2012, **134**, 17396-17399.

91. W. Abu Laban and L. Etgar, *Energy & Environmental Science*, 2013, **6**, 3249-3253.

92. J. B. You, Z. R. Hong, Y. Yang, Q. Chen, M. Cai, T. B. Song, C. C. Chen, S. R. Lu, Y. S. Liu, H. P. Zhou and Y. Yang, *Acs Nano*, 2014, **8**, 1674-1680.

93. S. B. Zhang, S. H. Wei, A. Zunger and H. Katayama-Yoshida, *Phys Rev B*, 1998, **57**, 9642-9656.

94. S. Y. Chen, X. G. Gong, A. Walsh and S. H. Wei, *Appl Phys Lett*, 2009, **94**, 041903.

95. W. J. Yin, S. H. Wei, M. M. Al-Jassim and Y. F. Yan, *Appl Phys Lett*, 2011, **99**, 142109.

96. G. C. Xing, N. Mathews, S. Y. Sun, S. S. Lim, Y. M. Lam, M. Gratzel, S. Mhaisalkar and T. C. Sum, *Science*, 2013, **342**, 344-347.

97. S. D. Stranks, G. E. Eperon, G. Grancini, C. Menelaou, M. J. P. Alcocer, T. Leijtens, L. M. Herz, A. Petrozza and H. J. Snaith, *Science*, 2013, **342**, 341-344.

98. A. S. Subbiah, A. Halder, S. Ghosh, N. Mahuli, G. Hodes and S. K. Sarkar, *J Phys Chem Lett*, 2014, **5**, 1748-1753.

99. P. Qin, S. Tanaka, S. Ito, N. Tetreault, K. Manabe, H. Nishino, M. K. Nazeeruddin and M. Gratzel, *Nature Communications*, 2014, **5**, 3834.

100. J. A. Christians, R. C. M. Fung and P. V. Kamat, *Journal of the American Chemical Society*, 2014, **136**, 758-764.

101. Anyi Mei, Linfeng Liu, Zhiliang Ku, Tongfa Liu, Yaoguang Rong, Mi Xu, Min Hu, Jiangzhao Chen, Ying Yang, Michael Grätzel, Hongwei Han, *Science*, 2014, **345**.

102. J. J. Shi, J. Dong, S. T. Lv, Y. Z. Xu, L. F. Zhu, J. Y. Xiao, X. Xu, H. J. Wu, D. M. Li, Y. H. Luo and Q. B. Meng, *Appl Phys Lett*, 2014, **104**, 063901.

103. S. Aharon, B. El Cohen and L. Etgar, *J Phys Chem C*, 2014, **118**, 17160-17165.

104. M. L. Agiorgousis, Y.-Y Sun, H. Zeng, and S. Zhang, *J. Am. Chem. Soc.*, 2014, **136**, 14570-14575.

105. J. J. Choi, X. H. Yang, Z. M. Norman, S. J. L. Billinge and J. S. Owen, *Nano Lett*, 2014, **14**, 127-133.

106. C. Li, Y. L. Wu, J. Poplawsky, T. J. Pennycook, N. Paudel, W. J. Yin, S. J. Haigh, M. P. Oxley, A. R. Lupini, M. Al-Jassim, S. J. Pennycook and Y. F. Yan, *Physical Review Letters*, 2014, **112,** 156103.

107. C. B. Feng, W. J. Yin, J. L. Nie, X. T. Zu, M. N. Huda, S. H. Wei, M. M. Al-Jassim and Y. F. Yon, *Solid State Communications*, 2012, **152**, 1744-1747.

108. W. J. Yin, Y. L. Wu, R. Noufi, M. Al-Jassim and Y. F. Yan, *Appl Phys Lett*, 2013, **102**, 193905.

109. W. J. Yin, Y. L. Wu, S. H. Wei, R. Noufi, M. M. Al-Jassim and Y. F. Yan, *Advanced Energy Materials*, 2014, **4,** 1300712.

110. E. Edri, S. Kirmayer, A. Henning, S. Mukhopadhyay, K. Gartsman, Y. Rosenwaks, G. Hodes and D. Cahen, *Nano Lett*, 2014, **14**, 1000-1004.

111. Y. Yan, C. S. Jiang, R. Noufi, S. H. Wei, H. R. Moutinho and M. M. Al-Jassim, *Physical Review Letters*, 2007, **99**, 235504.

112. I. Grinberg, D. V. West, M. Torres, G. Y. Gou, D. M. Stein, L. Y. Wu, G. N. Chen, E. M. Gallo, A. R. Akbashev, P. K. Davies, J. E. Spanier and A. M. Rappe, *Nature*, 2013, **503**, 509-+.

113. Y. Kutes, L. Ye, Y. Zhou, S. Pang, B. D. Huey, and N. P. Padture, *J. Phys. Chem. Lett.*, 2014, **5**, 3335-3339.

114. N. Pellet, P. Gao, G. Gregori, T. Y. Yang, M. K. Nazeeruddin, J. Maier and M. Gratzel, *Angewandte Chemie-International Edition*, 2014, **53**, 3151-3157.

115. F. Hao, C. C. Stoumpos, R. P. H. Chang and M. G. Kanatzidis, *Journal of the American Chemical Society*, 2014, **136**, 8094-8099.

116. S. Colella, E. Mosconi, P. Fedeli, A. Listorti, F. Gazza, F. Orlandi, P. Ferro, T. Besagni, A. Rizzo, G. Calestani, G. Gigli, F. De Angelis and R. Mosca, *Chem Mater*, 2013, **25**, 4613-4618.

117. S. A. Kulkarni, T. Baikie, P. P. Boix, N. Yantara, N. Mathews and S. Mhaisalkar, *Journal of Materials Chemistry A*, 2014, **2**, 9221-9225.

118. J. H. Noh, N. J. Jeon, Y. C. Choi, M. K. Nazeeruddin, M. Gratzel and S. I. Seok, *Journal of Materials Chemistry A*, 2013, **1**, 11842-11847.

119. P. Docampo, F. C. Hanusch, N. Giesbrecht, P. Angloher, A. Ivanova and T. Bein, *Apl Mater*, 2014, **2**, 081508.

120. Y. G. Rong, Z. L. Ku, A. Y. Mei, T. F. Liu, M. Xu, S. G. Ko, X. Li and H. W. Han, *J Phys Chem Lett*, 2014, **5**, 2160-2164.

121. R. S. Sanchez, V. Gonzalez-Pedro, J. W. Lee, N. G. Park, Y. S. Kang, I. Mora-Sero and J. Bisquert, *J Phys Chem Lett*, 2014, **5**, 2357-2363.

122. H. J. Snaith, A. Abate, J. M. Ball, G. E. Eperon, T. Leijtens, N. K. Noel, S. D. Stranks, J. T. W. Wang, K. Wojciechowski and W. Zhang, *J Phys Chem Lett*, 2014, **5**, 1511-1515.

123. E. Edri, S. Kirmayer, S. Mukhopadhyay, K. Gartsman, G. Hodes and D. Cahen, *Nature Communications*, 2014, **5**, 3461.

124. A. Abate, M. Saliba, D. J. Hollman, S. D. Stranks, K. Wojciechowski, R. Avolio, G. Grancini, A. Petrozza and H. J. Snaith, *Nano Lett*, 2014, **14**, 3247-3254.

125. B. Suarez, V. Gonzalez-Pedro, T. S. Ripolles, R. S. Sanchez, L. Otero and I. Mora-Sero, *J Phys Chem Lett*, 2014, **5**, 1628-1635.

126. E. Edri, S. Kirmayer, M. Kulbak, G. Hodes and D. Cahen, *J Phys Chem Lett*, 2014, **5**, 429-433.

127. E. Edri, S. Kirmayer, D. Cahen and G. Hodes, *J Phys Chem Lett*, 2013, **4**, 897-902.

128. G. Kresse and J. Furthmuller, *Physical Review B*, 1996, **54**, 11169-11186.

129. A. Zunger, S. H. Wei, L. G. Ferreira and J. E. Bernard, *Phys Rev Lett*, 1990, **65**, 353-356.

130. S. H. Wei, L. G. Ferreira, J. E. Bernard and A. Zunger, *Physical Review B*, 1990, **42**, 9622-9649.

131. S. H. Wei, L. G. Ferreira and A. Zunger, *Phys Rev B*, 1990, **41**, 8240-8269.

132. N. Kitazawa, Y. Watanabe and Y. Nakamura, *J Mater Sci*, 2002, **37**, 3585-3587.

133. L. G. Ferreira, S. H. Wei and A. Zunger, *Phys Rev B*, 1989, **40**, 3197-3231.

134. G. E. Eperon, S. D. Stranks, C. Menelaou, M. B. Johnston, L. M. Herz and H. J. Snaith, *Energy & Environmental Science*, 2014, **7**, 982-988.

135. F. C. Hanusch, E. Wiesenmayer, E. Mankel, A.Binek, P. Angloher, C. Fraunhofer, N. Giesbrecht, J. M. Feckl, W. Jaegermann, D. Johrendt, T. Bien, and P. Docampo, *J Phys Chem Lett*, 2014, **5**, 2791.

136. F. Hao, C. C. Stoumpos, D. H. Cao, R. P. H. Chang and M. G. Kanatzidis, *Nature Photonics*, 2014, **8**, 489-494.

137. N. K. Noel, S. D. Stranks, A. Abate, C. Wehrenfennig, S. Guarnera, A. A. Haghighirad, A. Sadhanala, G. E. Eperson, M. B. Johnston, A. M. Petrozza, L. M. Herz, and H. J. Snaith, *Energy & Environmental Science*, 2014, **7**, 3061.

138. M. Zhang, H. Yu, M. Lyu, Q. Wang, J.-H. Yun, and L. Wang, *Chemical Communications*, 2014, **50**, 11727-11730.

139. E. L. Unger, E. T. Hoke, C. D. Bailie, W. H. Nguyen, A. R. Bowring, T. Heumuller, M. G. Christoforo, and M. D. McGehee, *Energy & Environmental Science,* 2014,DOI: 10.1039/C4EE02465F.

Optical Absorptions of Typical Solar Cell Absorbers

Si *p,s*

E_g^i

Si *p*

weak
Indirect

Ga *s* + As *s*

E_g^d

As *p*

moderate
direct

Pb *p*

E_g^d

Pb *s* + I *p*

strong
direct

1st Generation   **2nd Generation**   **Perovskite halide**

First-principles calculations help to understand the fundamental mechanisms of the emerging perovskite solar cells and guide further developments.